# Delft University of Technology

## Comparison of macro x-ray fluorescence and reflectance imaging spectroscopy for the semi-quantitative analysis of pigments in easel paintings
### A study on lead white and blue verditer

de Almeida Nieto, Luís Manuel; Gabrieli, Francesca; van Loon, Annelies; Gonzalez, Victor; Dik, Joris; Van de Plas, Raf; Alfeld, Matthias

**Important note**
To cite this publication, please use the final published version (if applicable).
Please check the document version above.

RESEARCH ARTICLE

**X-RAY SPECTROMETRY** WILEY

# Comparison of macro x-ray fluorescence and reflectance imaging spectroscopy for the semi-quantitative analysis of pigments in easel paintings: A study on lead white and blue verditer

**Luís Manuel de Almeida Nieto**[1,2] | **Francesca Gabrieli**[3] |
**Annelies van Loon**[3] | **Victor Gonzalez**[4] | **Joris Dik**[1] |
**Raf Van de Plas**[2,5,6] | **Matthias Alfeld**[1]

[1]Department of Materials Science and Engineering, Delft University of Technology, Delft, The Netherlands

[2]Delft Center for Systems and Control, Delft University of Technology, Delft, The Netherlands

[3]Science Department, Conservation and Science, Rijksmuseum, Amsterdam, The Netherlands

[4]Université Paris-Saclay, ENS Paris-Saclay, CNRS, PPSM, Gif-sur-Yvette, France

[5]Department of Biochemistry, Vanderbilt University, Nashville, Tennessee, USA

[6]Mass Spectrometry Research Center, Vanderbilt University, Nashville, Tennessee, USA

**Correspondence**

Luís Manuel de Almeida Nieto, Department of Materials Science and Engineering, Mekelweg 2, 2628 CD Delft, The Netherlands.
Email: l.m.dealmeidanieto@tudelft.nl

## Abstract

Macroscopic x-ray fluorescence imaging spectroscopy (MA-XRF) and reflectance imaging spectroscopy (RIS) are important tools in the analysis of cultural heritage objects, both for conservation and art historical research purposes. The elemental and molecular distributions provided by MA-XRF and RIS respectively, are particularly useful for the identification and mapping of pigments in easel paintings. While MA-XRF has relatively established data processing methods based on modeling of the underlying physics, RIS data cannot be modeled with sufficient precision and its processing has considerable room for improvements. This work seeks to improve RIS data processing workflows in the short wavelength infrared range (SWIR, 1000–2500 nm) with a novel method that fits Gaussian profiles to pigment-specific absorption features, and we compare its performance to MA-XRF for the task of semi-quantitative pigment mapping, evaluating their limits of detection (LODs) and the matrix effects that affect their signals. Two pigments are considered in this work, lead white and blue verditer, which are mapped in SWIR RIS using the first overtone of —OH stretching of their primary compounds, hydrocerussite $(Pb_3(CO_3)_2(OH)_2)$ and azurite $(Cu_3(CO_3)_2(OH)_2)$, at 1447 and 1497 nm respectively, and in MA-XRF using the Pb-L and Cu-K fluorescence signals. The methods are evaluated using two sets of custom-prepared paint samples, as well as a 16th-century painting, discussing the identification, mapping, and semi-quantitative analysis of the considered pigments. We found SWIR RIS to be a pigment-specific method with a longer linear range but inferior LODs and penetration depth when compared to MA-XRF, the latter is often not capable of discriminating between different pigments with identical elemental

markers. We furthermore present a novel color scale that allows the simultaneous visualization of signals above and below a confidence limit.

# 1 | INTRODUCTION

Paintings are, from a material point of view, highly heterogeneous systems consisting of many unevenly distributed paint layers. Each paint layer consists of a heterogeneous mixture of pigments that have the strongest contribution to the perceived color, a binder that holds the paint together; and potentially any other additives that modify other characteristics of the paint, such as its viscosity or drying speed. The combined heterogeneity of paintings mandates the use of techniques that provide spatially resolved chemical information. In recent years, two such imaging techniques, macroscopic x-ray fluorescence imaging spectroscopy (MA-XRF) and reflectance imaging spectroscopy (RIS) have become routine tools for the analysis of historical paintings and other cultural heritage objects. They contribute to conservation and art historical research by identifying pigments and visualizing their distribution.[1–9]

MA-XRF reveals distributions in samples by recording characteristic radiation emitted during inner shell electronic transitions upon stimulation by a primary x-ray beam. The underlying physics of XRF are well understood and modeled, such that element-specific distribution images can be readily obtained.[10] However, its limitation to elemental information prevents it from delivering conclusive pigment identification, as distinct pigments can share an elemental footprint. Examples are azurite ($Cu_3(CO_3)_2(OH)_2$) and malachite ($Cu_2CO_3(OH)_2$) whose single elemental marker is Cu.

In the visible and infrared spectral ranges, RIS measures the light reflected or scattered by a sample, supplying information on the molecules present in the material, and delivering insight complementary to information provided by MA-XRF. RIS in the visible range (commonly the visible to near-infrared range in commercial cameras, VNIR, from 350 to 1000 nm) may provide information on the electronic transitions of molecules occurring in that spectral range, which can provide insight as to the visible color of some compounds. RIS in the short wavelength infrared range (SWIR; from 1000 to 2500 nm), which is the focus of this research, provides information on the distribution of many chemical species using characteristic frequencies related to vibrational

modes of certain functional groups, like O—H.[11] However, modeling of the reflectance response of complex material matrices, like paint layers, in the SWIR spectral range is challenging,[12,13] making the extraction of chemical distribution maps from SWIR RIS data more difficult than for MA-XRF. Novel methods have also been described for RIS in certain sections of the mid-infrared range (MIR, from 2500 to 25,000 nm), like 2500–3750 nm in[14] and 8064–13,158 nm in,[15] which provides access to even further vibrational modes, such as C—H and C—O, respectively. However, these have not yet seen widespread use.

Currently, most RIS data processing methods used in cultural heritage science revolve primarily around dimensionality reduction methods, such as principal component analysis (PCA), t-distributed stochastic neighbor embedding (t-SNE),[16] or uniform manifold approximation and projection (UMAP),[17,18] followed by manual endmember selection and a mapping approach, such as spectral angle mapping (SAM).[19,20] While these methods are commonly used in the analysis of RIS datasets (in particular for the VNIR range, presenting less sharp spectral features), their unsupervised machine-learning nature makes the results often dataset-specific and the manual user intervention steps tend to be rather labor–intensive, and difficult to reproduce. Recently, more automated approaches based on artificial neural networks and other spectral matching algorithms have been successfully demonstrated[21-24] but have not yet seen widespread use in the routine analysis of RIS data from paintings.

This paper describes an approach for SWIR RIS data processing that enables the spatial mapping and semi-quantitative evaluation of pigments, namely a confirmation of pigment presence and an estimation of the pigment's areal density, through the vibrational spectral features they present in the SWIR spectral range.

We demonstrate our data workflow and focus our study on two specific pigments: lead white (abbreviated as LW) (typically a mixture of lead carbonates, hydrocerussite $Pb_3(CO_3)_2(OH)_2$, and cerussite $PbCO_3$[25]), and blue verditer (abbreviated as BV) (a hydrated copper carbonate $Cu_3(CO_3)_2(OH)_2$, the synthetic equivalent of azurite[26]). These two pigments were chosen due to their
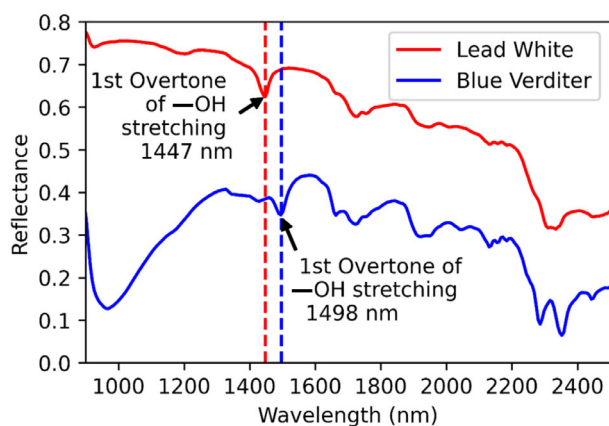
**FIGURE 1** Short wavelength infrared (SWIR) reflectance spectra for lead white (LW) and blue verditer (BV) taken from their respective 150 μm single-pigment samples, and the fitting reflectance feature of each.

widespread use in historical paintings and their useful absorption features in the SWIR range. Our proposed method consists of fitting a Gaussian profile in the RIS spectrum onto the characteristic absorption features of the two pigments. For lead white, we use the first overtone of —OH stretching of hydrocerussite, which is centered around 1447 nm.[27] For blue verditer, we use the first overtone of —OH stretching of azurite centered around 1497 nm.[28] The SWIR RIS spectra of both pigments and their corresponding absorbance features can be seen in Figure 1. A similar method was employed by De Meyer et al.[27] for the analysis of SWIR RIS data but was limited to the qualitative mapping of hydrocerussite.

MA-XRF and the Gaussian fitting approach to SWIR RIS features (shown in Figure 2) are evaluated for their potential for semi-quantitative pigment-specific mapping. The evaluation entails the pigment analysis of three objects: two sets of custom-made paint mock-ups (mixture and layered systems), which allow for the evaluation with regards to both pigment identification and semi-quantitative analysis, and a 16th-century panel painting, which provides a practical example for pigment identification. The potential for semi-quantitative pigment analysis is benchmarked by comparing the intensity of each pigment's characteristic signals in each method (i.e., for blue verditer, Cu-Kα for MA-XRF, and azurite for SWIR RIS) to the pigment areal density of each sample. Whilst MA-XRF and RIS do not always directly measure the pigments themselves, but rather components thereof (elements for MA-XRF and chemical species for RIS), and given that the measured response for each modality reports a different property and covers a different dynamic range, all quantitative results are translated into pigment areal density values that enable direct

comparison between the two methods in terms of quantitation.

## 2 | MATERIALS AND METHODS

### 2.1 | Test samples

Two sets of paint mock-ups were prepared to evaluate and compare the methods for different paint layer compositions and structures. These two sets were both made using three pigments: lead white (LW), blue verditer (BV), and yellow ochre (YO). All pigments were sourced from Rublev Colors (Willits, CA) (Full pigment analysis available in Figures S1–S3 and Tables S1, S2). These pigments were selected due to their distinct elemental footprints and characteristic absorption features. In MA-XRF, blue verditer can be detected by means of the Cu-K fluorescence lines, and in SWIR RIS by the first overtone of —OH stretching (1497 nm), combination $\nu + \delta$ (stretching and bending) of —OH (2285 nm) and second overtone of $-CO_3^{-2}$ stretching (2352 nm) of azurite[28] (spectra shown in Figure 1). Lead white, which in this case is a mixture of 98% hydrocerussite and 2% cerussite, can be detected through MA-XRF by observing the Pb-L and Pb-M fluorescence lines, and in SWIR RIS by the first overtone of —OH stretching (1447 nm) and combination $\nu + \delta$ of —OH and second overtone of $-CO_3^{-2}$ stretching (2325 nm) of hydrocerussite[27,29] (spectra shown in Figure 1). Only the features in the 1400–1500 nm range were used in this research, as this is the range in which the binder (linseed oil) is least likely to present strong absorption features. While the yellow ochre pigment used in these experiments can be detected through SWIR RIS due to the presence of kaolinite ($Al_2(OH)_4Si_2O_5$) as a secondary component through two absorption bands of the first overtone of —OH stretching (1396 nm and 1415 nm),[30] the main coloring component, goethite (α-FeO(OH)), lacks characteristic absorption features in the SWIR spectral range and consequently the pigment is not regarded in the subsequent text.

All paints were ground by hand with a muller on a glass plate, using raw linseed oil (Kremer Pigments Inc., New York, NY) as a binder at oil mass ratios of 14%, 22%, and 29%, respectively for lead white, blue verditer, and yellow ochre. The paints were applied on 50 μm Melinex film using a metal 4-sided Bird-type film applicator. After drying, the samples were attached to a 3 mm plexiglass sheet for rigidity. The reflectance spectrum and XRF signals of the support material are provided in Figures S4, S5 and Table S4.

The first set of paint mock-ups is a collection of single-layer samples, hereafter referred to as the mixture
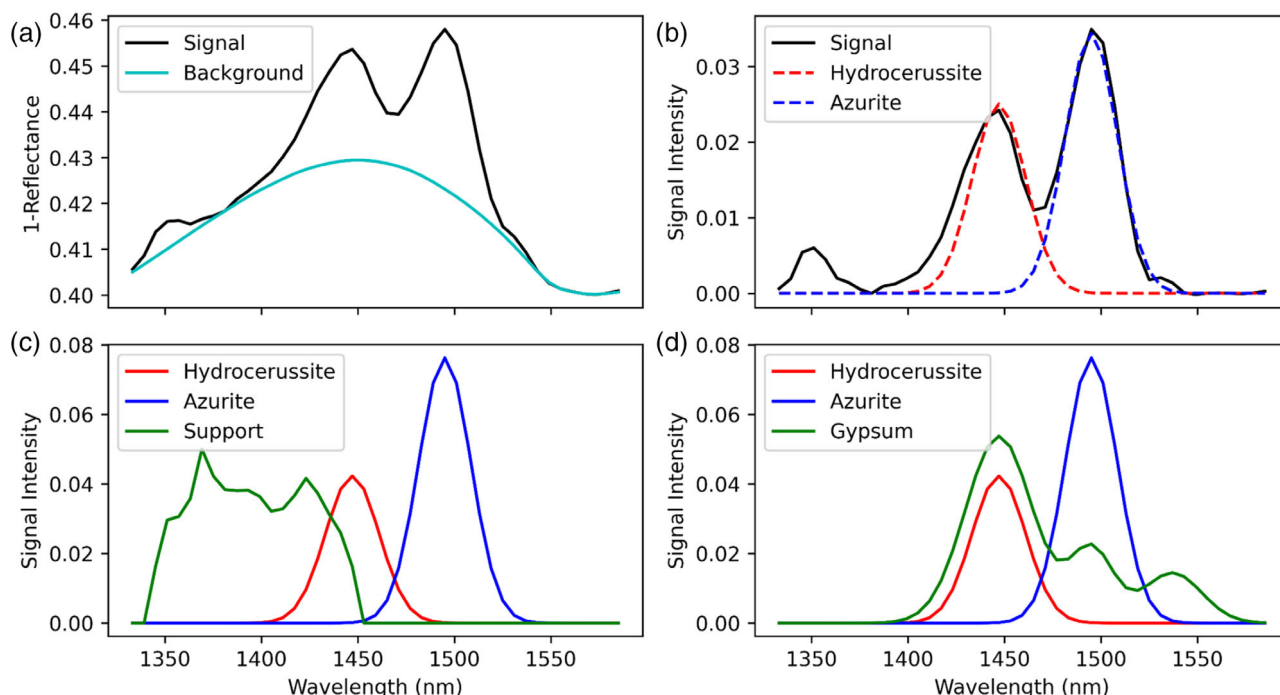
**FIGURE 2** (a) Inverted reflectance spectra from a 50/50 BV/LW 150 μm paint sample and the calculated background. (b) Processed RIS signal and two Gaussian profiles fit onto the absorbance features. (c) Fitting components used for the fitting of the paint mock-ups. (d) Fitting components used for the fitting of the test painting.



**FIGURE 3** Mixture samples of lead white (LW), blue verditer (BV), and yellow ochre (YO). (a) Visible photograph. The three different mixtures are marked. Each mixture includes five mixture ratios (5%, 20%, 50%, 80%, and 95%). All samples in each row have the same layer thickness, marked on the left. (b) Macroscopic x-ray fluorescence imaging spectroscopy (MA-XRF) Pb-Lα map. (c) MA-XRF Cu-Kα map. (d) MA-XRF Pb-M map. (e) RIS azurite map. (f) RIS hydrocerussite map. All maps are displayed with the signals below the LODs in greyscale, and the signals above the LODs in a yellow-red heatmap.
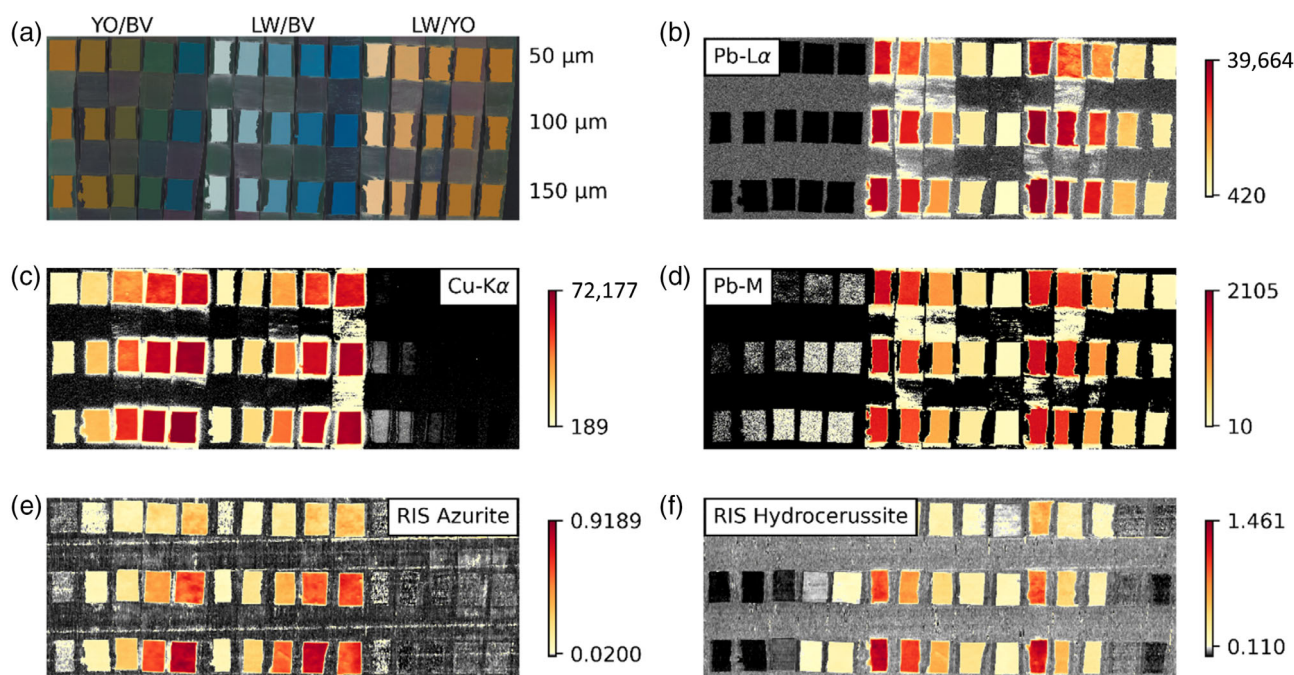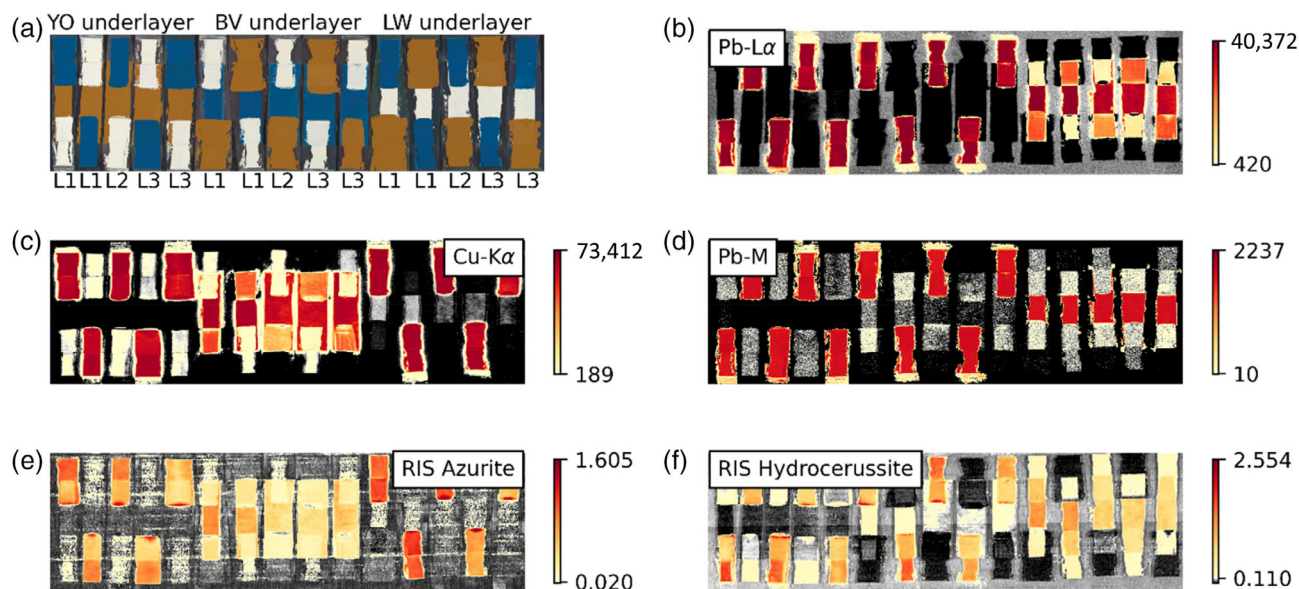
**FIGURE 4** Layer samples of lead white (LW), blue verditer (BV), and yellow ochre (YO). (a) Visible photograph. Three different layer sample configurations are marked: L1 (50 μm over 100 μm), L2 (100 μm over 50 μm), and L3 (50 μm over 50 μm). (b) Macroscopic x-ray fluorescence imaging spectroscopy (MA-XRF) Pb-Lα map. (c) MA-XRF Cu-Kα map. (d) MA-XRF Pb-M map. (e) RIS azurite map. (f) RIS hydrocerussite map. All maps are displayed with the signals below the LODs in greyscale, and the signals above the LODs in a yellow-red heatmap.

samples (Figure 3a). Each of these samples was put down as a single paint layer, where the used paint was a mixture of two single-pigment paints at a specific mass ratio. The ratios examined were 5:95, 20:80, 50:50, 80:20, and 95:5 and each paint ratio was applied in three different nominal layer thicknesses (50, 100, and 150 μm). The second mock-up set is a collection of double-layered samples, hereafter referred to as the layer samples (Figure 4a). Each of these samples was made by first applying a layer of paint of one type of pigment, letting it dry for a week, and then applying another layer of different single-pigment paint. The samples were applied in three thickness combinations: 50 μm over 100 μm (L1), 100 μm over 50 μm (L2), and 50 μm over 50 μm (L3). The paint layers were applied such that for both the top and bottom layers an area of no overlap was present, leaving single-layer areas accessible with three thicknesses (50, 100, and 150 μm). These thicknesses of single paint layers were achieved as in the absence of a second layer the single layer thickness is the sum of the nominal thicknesses of both layers (e.g., 100 μm for the L3 samples). Figure 5 provides a visual diagram of the paint layer build-up. Each sample on both sets has an area of roughly 2 × 3 cm². All samples were allowed to dry for a month before measurements started. A full description of the sample compositions is available in Figures S6, S7 and Tables S5, S6.

MA-XRF and SWIR RIS were also applied to the analysis of Jacob Cornelisz van Oostsanen's *Portrait of Jan Gerritsz van Egmond van de Nijenburg* (oil on panel, h 42.4 cm × w 32.8 cm, c. 1518), from the Rijksmuseum Collection (SK-A-3838) (Figure 6a). Given the painting's shape and non-removable frame, only a section of the painting was scanned with MA-XRF to avoid potential collisions between the frame and the MA-XRF measurement head. This painting was analyzed in relation to conservation work in preparation for an upcoming exhibition. The analysis confirmed the presence of both azurite and lead white, making it the perfect test case for our novel mapping method.

## 2.2 | Data acquisition and processing

### 2.2.1 | Ma-XRF

MA-XRF data were acquired using an M6 Jetstream MA-XRF scanner equipped with two 60 mm² SDD detectors (Bruker Nano GmbH, Berlin, Germany).[31] The Rhodium x-ray tube was operated at 50 kV and 200 μA, and the scan was conducted with a dwell time of 400 ms and a step size of 500 μm for the paint mock-ups and a dwell time of 70 ms and a step size of 450 μm for the painting. This resulted in data sets of 342 × 892 pixels for the
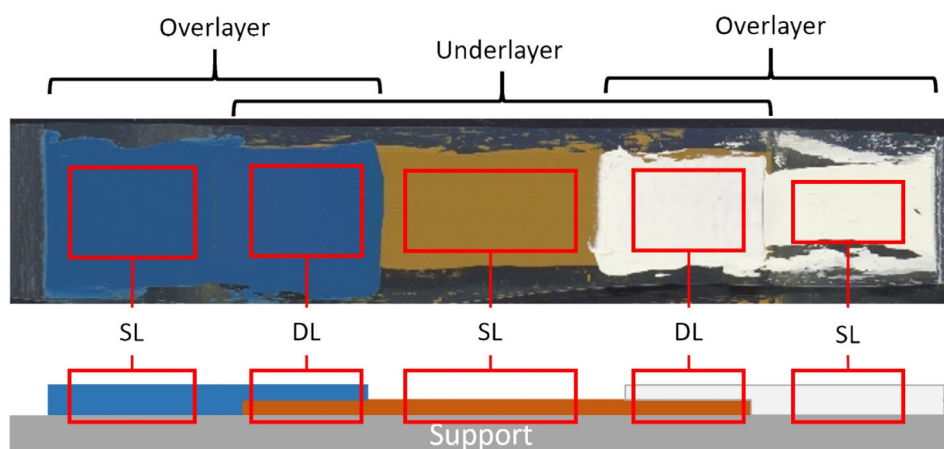
**FIGURE 5** Cross-section diagram of the paint layer build-up of the layer samples. SL are single-layer samples and DL are double-layer samples.

mixture samples, 372 × 1232 pixels for the layer samples, and 485 × 374 pixels for the painting. The spectral data were processed using DataMuncher[32] and PyMCA[33] to produce elemental signal intensity maps.

To evaluate the potential for semi-quantitative analysis, the arithmetic means of signal intensities of each paint sample were taken and compared to the known pigment areal density of each sample. To determine the limits of detection (LODs), the critical signal value $y_c$ was calculated using Equation 1, where $\bar{y}_{BL}$ is the average blank signal and $s_{BL}$ is the standard deviation of the blank signal.[34] The blank signal was taken from areas of the data set where each considered pigment is not present.

$$y_c = \bar{y}_{BL} + 3s_{BL} \qquad (1)$$

For these datasets, it was observed that the relationships between signal intensity and areal density for the single layer 50 µm samples of both pigments were approximately linear. This happens since the samples are thin enough for matrix effects to not play a very prominent role in signal intensity. A linear fit of these 50 µm samples was used to describe these relations and the areal density value at which this linear fit crosses $y_c$ was taken as the LOD. An alternative, more traditional method of calculating the LODs for MA-XRF compares the intensity of a fluorescence signal to its spectral background[31] using:

$$\text{LOD} = 3\frac{\sqrt{N_{\text{back}}}}{N_{\text{signal}}}c\sqrt{t} \qquad (2)$$

where $N_{\text{back}}$ and $N_{\text{signal}}$ are the background and peak intensities, respectively, $c$ is the elemental concentration and $t$ is the measurement time. However, in the context of this paper, we prefer the first method since it can also

be applied to SWIR RIS, and therefore can yield a more direct comparison.[31]

## 2.2.2 | SWIR RIS

SWIR RIS data was acquired using a Micro-Hyperspec SWIR 640 hyperspectral camera (Headwall Photonics, Boston, MA), covering a spectral range from 900 to 2500 nm, with a spectral resolution of 6 nm (267 channels) and a custom-built motorized easel (LG Motion, Basingstoke, UK). The samples were illuminated by two Gulliver 30 lamps (Ianiro LED, New Taipei City, Taiwan) with 150 W halogen 3000 K bulbs set at 50° of the surface normal. The camera was operated using an integration time of 120 ms per line. The datasets were calibrated using a Spectralon 99% diffuse white reflectance standard (Labsphere, North Sutton, NH). The mixture samples were too large to be acquired in a single scan, and thus two scans were taken and later stitched together using DataHandlerP.[35] The datasets were scaled to match the resolution of the MA-XRF scans, resulting in datasets of 342 × 892 pixels for the mixture samples and 357 × 1232 pixels for the layer samples, with a pixel size of approximately 500 µm. The painting was also too large for a single scan acquisition, and instead four scans were stitched together, resulting in a dataset of 3250 × 2170 pixels with a pixel size of ∼168 µm.

To be able to fit the reflectance features, the data needed to be pre-processed. First, the data set was cropped to the desired spectral range (1333–1591 nm). Then, a 5-pixel special median filter perpendicular to the scanning direction was used to get rid of single-pixel measurement artifacts, followed by a Savitzky–Golay filter (window length of 5 and polynomial degree of 2) in the spectral direction to reduce noise and smooth the SWIR spectral profile. The flat-field normalized reflectance signal (R) was then inverted (1-R). Afterward, the
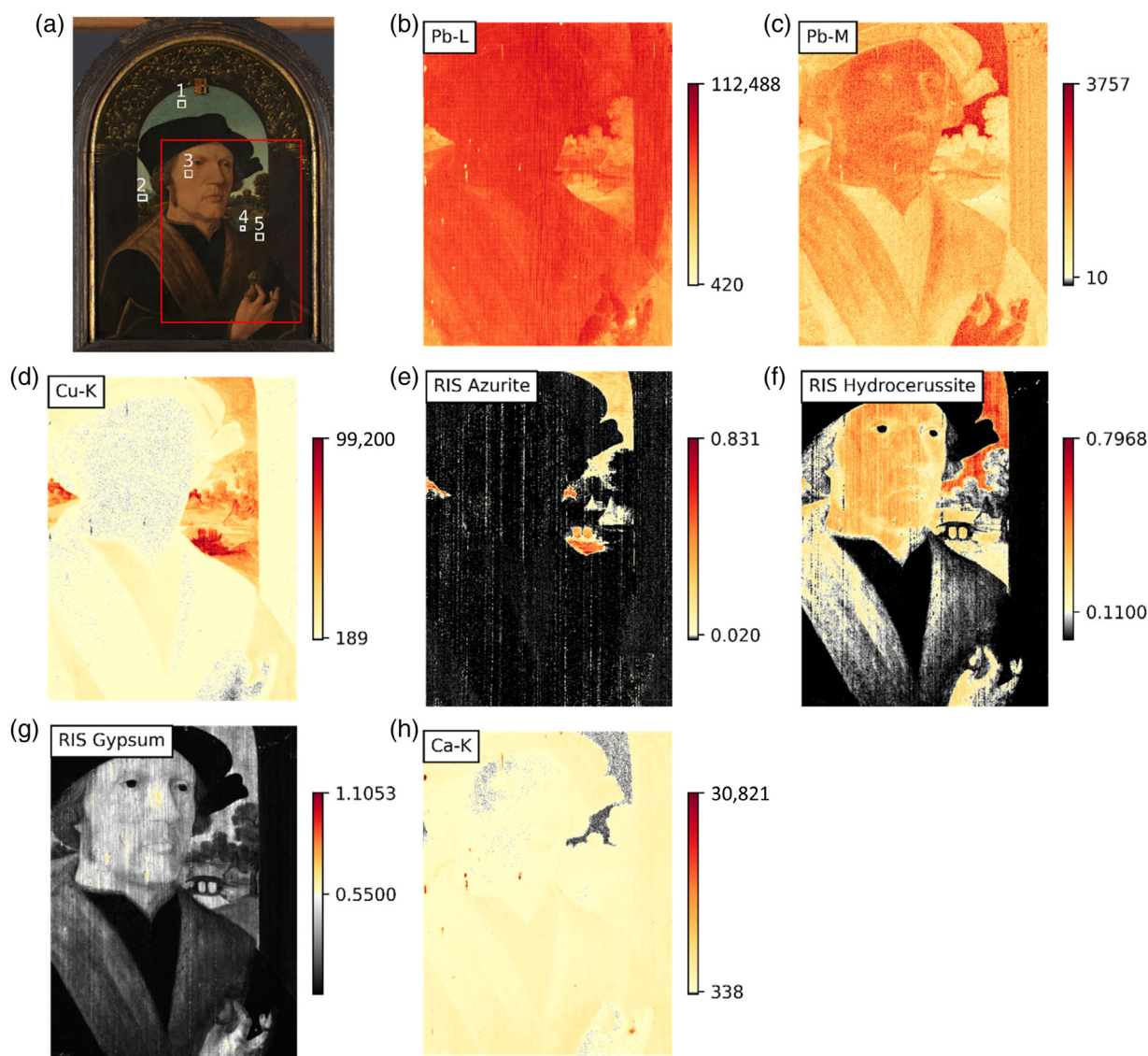
**FIGURE 6** Jacob Cornelisz van Oostsanen, Portrait of Jan Gerritsz van Egmond van de Nijenburg, c. 1518, oil on panel, h 42.4 cm × w 32.8 cm, Rijksmuseum (SK-A-3838) (a) Visible light photograph with the MA-XRF scanned area marked in red and areas used for SWIR RIS calculations in white. (b) MA-XRF Pb-L map. (c) MA-XRF Pb-M map. (d) MA-XRF Cu-K map. (e) RIS azurite map. (f) RIS hydrocerussite map. (g) RIS gypsum map. (h) MA-XRF Ca-K map. All maps are displayed with the signals below the LODs in greyscale, and the signals above the LODs in a yellow-red heatmap. RIS maps are cropped to show only the area scanned with MA-XRF, full maps are available in Figure S15.

specific features were isolated from the background absorption using a variant of the SNIP filter,[36] as shown in Figure 2a. The initial half-window size for the SNIP filter depends on the width of the absorbance features being studied and is traditionally set as approximately half the width of the target feature. Following this, a half-window size of six was used for this research and was found to provide reliable feature isolation. After the pre-processing, the fitting of features is done using the SciPy Non-negative Least Squares fitting (NNLS) function provided through DataHandlerP. The Gaussian profiles used for the fitting of spectral features are derived from the 150 μm single-pigment samples. Spectra from these samples were pre-processed as described above, and then the width and height of the Gaussian profiles were calculated using the SciPy *curve_fit()* function.[37] These profiles are shown in Figure 2b. Gaussian profiles were initially chosen due to their simplicity and were found to provide satisfying fits to the considered absorption features, as the background removal forces the peaks to have very short tails. Since the support material used for the paint mock-ups also has a broad absorption feature slightly overlapping with the hydrocerussite feature, it was required to include a third component during the fitting (Figure 2c).

This component was taken directly from the processed data. A similar issue occurred with the painting, where the presence of gypsum ($CaSO_4 \cdot 2H_2O$) in areas of restoration caused problems during the fitting due to its triple absorption features at 1445, 1490, and 1535 nm.[19] The first two features overlap directly with those of hydrocerussite and azurite, respectively, and thus cause significant issues with the identification. To account for that, a third component was added for gypsum (Figure 2d). The component was derived using a method similar to that used for the other components but using a function consisting of 3 Gaussian profiles of which the height and width are calculated using the curve_fit function on a sample spectrum extracted from the painting's data set.

For the semi-quantitative analysis and calculation of SWIR LODs, an approach similar to that used for MA-XRF signals was utilized on the SWIR signals, with the mean signal intensities of each paint sample being compared to pigment areal density.

To clearly show which areas of an elemental or chemical map are above or below its corresponding limit of detection we devised a non-standard color scheme in that signals above the LOD are shown in a red-orange heat map and signals below in a greyscale. The signals depicted in the red-orange colormap can be labeled as detected. While signals that fall below a conservatively set LOD (with the LOD only considering spectral information and not spatial information) cannot be labeled as reliably detected, their distribution often still reports genuine pigment distribution traces and thus still allows for low-abundant pigment distributions to be discerned. The combined color scale allows for a clear visual distinction between reliably detected and sub-LOD signals, but also still yields a way for spatial pigment distributions to be discerned regardless of whether the LOD threshold is met in all pixel locations.

# 3 | RESULTS

## 3.1 | Paint samples

### 3.1.1 | Ma-XRF

For the paint mock-ups, the elemental distribution maps for Cu-Kα (8.0 keV), Pb-Lα (10.6 keV), and Pb-M (0.6–3.7 keV) are used (All other MA-XRF maps are presented in Figures S8–S11). These specific lines are chosen as they are the most intense of their respective electron shells. For the single-layer samples, the MA-XRF maps (Figure 3b–d) reliably confirm the elemental presence of the considered pigments. In the case of the layer samples (Figure 4b–d), the presence of overlying layers does affect the elemental signal intensity from underlying layers, but the extent of this effect depends mostly on both the fluorescence energy of the underlying layer and how strongly absorbing the overlying layer is with regards to that fluorescence energy. For example, comparing the signal intensity ($I$) of an uncovered $100\,\mu m$ blue verditer layer to the signal intensity of such a layer covered by an overlying $50\,\mu m$ yellow ochre layer it is found that the covered Cu-Kα signal is only 69.7% ($= I_{covered}/I_{uncovered}$) of the intensity of the uncovered signal. For an overlying $50\,\mu m$ lead white layer, the Cu-Kα signal is reduced to 3.3% of the uncovered signal intensity.

As for semi-quantitative analysis, in Figure 7a,b the average sample signal intensities of the considered fluorescence lines are plotted against the areal density of the corresponding pigments. The results suggest a discernable relationship between signal intensity and pigment areal density. However, as expected, this relationship varies significantly in function of several factors such as the overall pigment concentration, the presence of other pigments, and their mass absorption coefficients, which influences absorption within the sample. All of these are well-documented factors common to quantitative XRF analysis.[10]

One notable exception to this trend is the Pb-M fluorescence lines (Figures 3d and 4d), a group of low energy (0.6–3.7 keV) and low intensity (~50 times less than Pb-Lα) fluorescence lines, which are very strongly absorbed by the samples, and are therefore only related to superficial Pb presence. Since the signal from these fluorescence lines is only related to a very thin section of the surface, matrix effects play much less of a role in the investigated samples, and the signal is therefore much more strongly correlated to Pb concentration at the surface of the paint layer, as can be seen in Figure 7c. Any material beyond the first 13 μm of a lead white paint layer is not expected to contribute significantly to the Pb-M signal, as only around 0.5% of the radiation at 2.3 keV, the energy of the strongest Pb-M line, is able to escape (as shown in Figure S12).

The calculated LODs (using the Cu-K and Pb-L lines) are of $0.04\,mg/cm^2$ for blue verditer and $0.30\,mg/cm^2$ for lead white, which are equivalent to $0.02\,mg/cm^2$ of Cu and $0.24\,mg/cm^2$ of Pb, respectively. Using the Pb-M lines, the surface-specific LODs are $0.03\,mg/cm^2$ for lead white, which is equivalent to $0.02\,mg/cm^2$ of Pb. Using Equation 2, the LODs for the $100\,\mu m$ 50% blue verditer/50% lead white sample were calculated as 0.04 and $0.10\,mg/cm^2$ for Cu and Pb, respectively. These results are in good agreement with those reported by Alfeld et al.,[31] which reported 90 ppm of Cu for a NIST SRM 610 (density: $2.5\,g/cm^3$, thickness: 1 mm), which is equivalent to $0.03\,mg/cm^2$ of Cu.
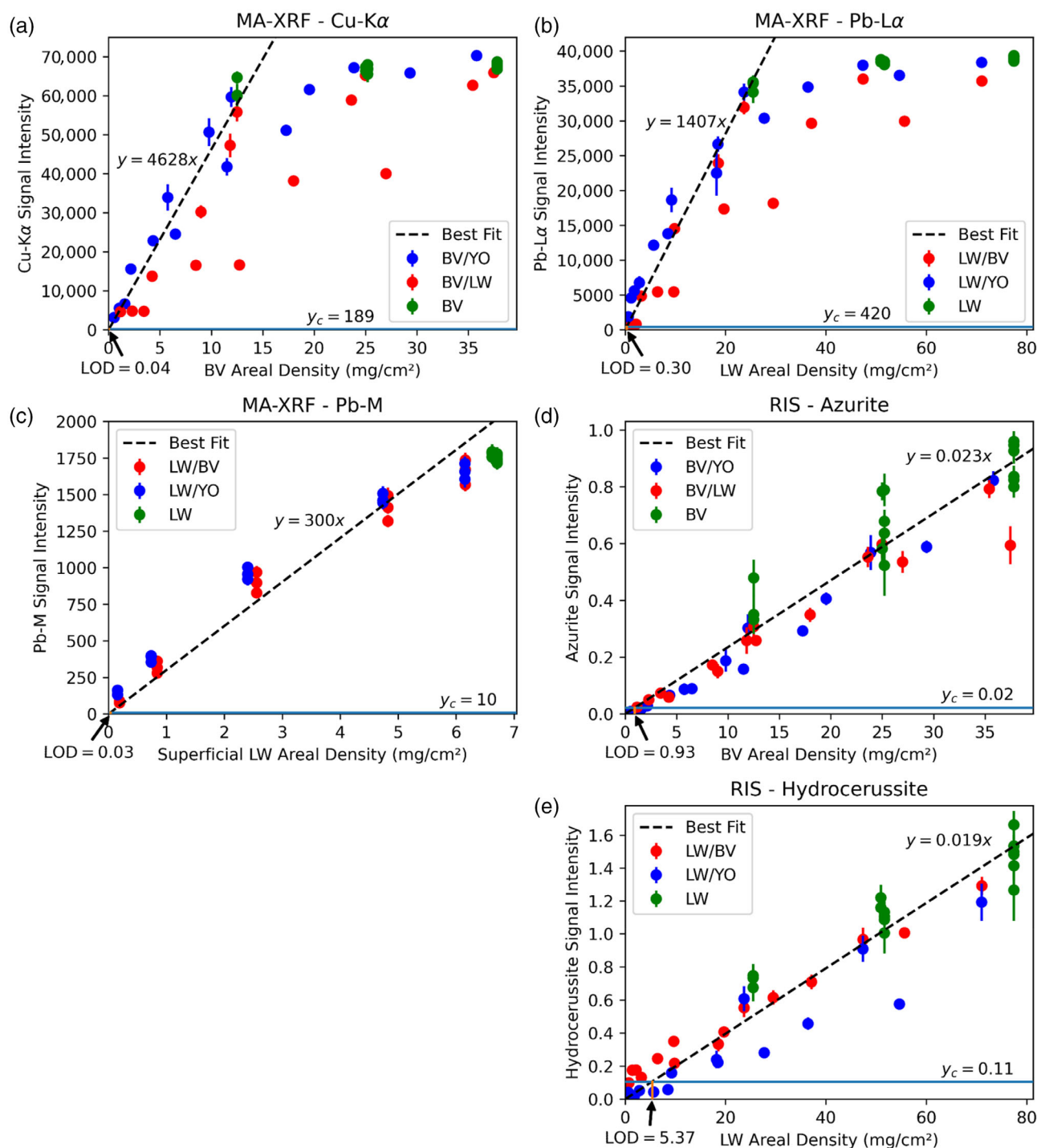
**FIGURE 7** Relationship between signal intensities and pigment areal densities and calculated limits of detection for (a) Macroscopic x-ray fluorescence imaging spectroscopy (MA-XRF) Cu-Kα, (b) MA-XRF Pb-Lα, (c) MA-XRF Pb-M, (d) Reflectance imaging spectroscopy (RIS) azurite, (e) RIS hydrocerussite. Error bars represent the standard deviation of the related signal intensities across each paint sample.

## 3.1.2 | SWIR RIS

The method manages to produce fairly accurate pigment distribution maps, shown in Figures 3e,f and 4e,f, but it sometimes struggles with identifying the compounds when they are minor components (<20 mass%) of a mixture. In the layer samples (Figure 4e,f), it is seen that the signals from underlying layers tend to be attenuated by overlying layers, the extent of which again depends on the nature of the overlying layer. For example, using the same comparison method as during the MA-XRF analysis, a 100 μm blue verditer layer has its signal attenuated

to 29% of the uncovered signal intensity by an overlying 50 μm yellow ochre layer and to 46% by an overlying 50-μm lead white layer. Again, the difference between blue verditer and lead white reappears with the method being able to identify blue verditer in all layer configurations, but not lead white. In both datasets, areas with large concentrations of azurite present a hydrocerussite signal, which means the method is more reliable for the identification of blue verditer than for lead white.

Regarding semi-quantification, Figure 7d,e shows the average sample signal intensity plotted against the areal density of the corresponding pigments. The relationship between the SWIR RIS signal intensity and the pigment areal density in the single-layer samples is much better described by a linear fit than for MA-XRF. The azurite results show a closer correlation than the hydrocerussite results, but this could be due to the previously mentioned azurite misidentifications or due to the overlap between the support and kaolinite features and the hydrocerussite feature.

The calculated LODs are 0.93 mg/cm$^2$ for blue verditer and 5.37 mg/cm$^2$ for lead white, which are equivalent to 0.93 mg/cm$^2$ of azurite and 5.26 mg/cm$^2$ of hydrocerussite, respectively.

## 3.2 | Application to a painting

In the selected painting by Jacob Cornelisz van Oostsanen, the Pb-L map (Figure 6b) reports the presence of Pb over the entire painting, except for small areas of restoration, implying the use of a lead white priming layer. As mentioned before, the Pb-M map (Figure 6c) is surface-specific and therefore shows the presence of Pb also on the surface paint layers throughout most of the painting, but most predominantly in the sky in the background and in the skin of the figure. Cu (Figure 6d) was identified in the landscape background, most intensely in the water and rearmost section of trees, and less intensely in the clothing of the figure. Other MA-XRF maps of the painting are presented in Figures S13 and S14.

The azurite signal (Figure 6e) is identified in amounts above the LOD in the background in the water, the sky, and the rearmost section of trees. Other areas show azurite signals below the LOD, but they are not highly spatially correlated, implying they are likely due to measurement noise. A hydrocerussite signal (Figure 6f) above the LOD is present in the open sky in the background and the skin of the figure, whilst signals below the LOD appear in the other sections of the outdoor background, a section of the background arch and the fur vest of the figure.

Since a component for gypsum was included in the fitting, a map for this feature could be produced as well (Figure 6g). This gypsum signal is present most intensely in areas of restoration, where it was used to fill the long cracks which formed along the direction of the wood grain of the supporting panel, a common practice in the restoration of panel paintings. The signal is also mapped in other areas of the painting, with a strong correlation to the areas with a hydrocerussite signal. The Ca-K maps produced with MA-XRF (Figure 6h) show the presence of Ca in similar areas of restoration, but a low-intensity Ca-K signal is also present in the clothing of the figure and darker areas of the background. Lacking a reference sample, which could be used to determine the LODs for gypsum and Ca, an area of the painting was used to determine the blank signal. The area used was the small area of open sky between the figure's face and the trees on the right, as this was the area with the lowest Ca-K signal.

## 4 | DISCUSSION

Regarding pigment identification, SWIR RIS yields mixed results. It mostly compares well with the results achieved with MA-XRF, but notable differences are apparent. In the mixture samples (Figure 3), SWIR RIS method struggles to identify either azurite or hydrocerussite (Figure 3e,f) when they are present in amounts close to the LODs, the values of which are poor (higher LOD values) compared to those achievable with MA-XRF (Figure 3b–d). This can be seen in several of the samples including 5% of either blue verditer or lead white which are not correctly mapped. However, in the samples with larger blue verditer (>50 mg/cm$^2$) and lead white (>25 mg/cm$^2$) areal densities, MA-XRF fails to clearly differentiate between samples of different thickness, as the samples approach infinite thickness from the point of the discussed XRF lines, as can be seen in Figure 7a,b. The SWIR RIS method does manage to differentiate between these samples, showing a greater information depth, which is the depth that provides 99.5% of the measured signal in an infinitely thick sample. However, the exact information depth cannot be accurately determined as it seems to exceed the maximum tested layer thickness of 150 μm.

For reference, paint layers are often between 10 and 100 μm,[38] which, assuming similar oil ratios as those recommended by modern suppliers, would equate to between 2.5 and 25 mg/cm$^2$ for a pure blue verditer paint and 5.1–51 mg/cm$^2$ for a pure lead white paint. Given that these pigments are often used in mixtures, common
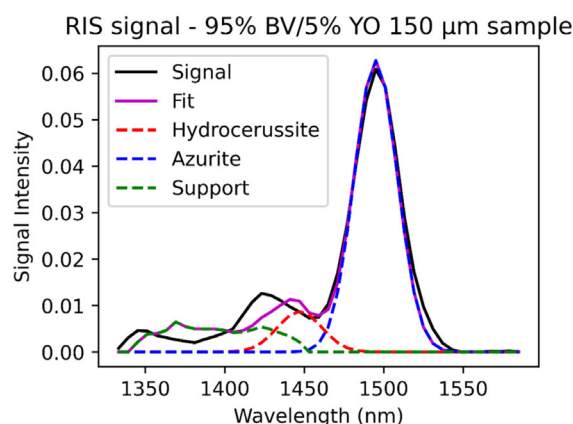
**FIGURE 8** Spectra example showing the fitting of a small hydrocerussite signal in a sample without hydrocerussite (Mixture sample, 95% blue verditer/5% yellow ochre, 150 μm).

areal density values are expected to be lower. However, lead white is commonly used as a ground, often resulting in much thicker layers[39] and therefore higher areal densities.

The layer samples (Figure 4) mostly support prior observations, as not only the method differentiates between the different layer thicknesses, but also the areas where the film applicator pooled the paint into thicker layers have much stronger SWIR RIS signals than the rest of the samples (Figure 4e,f). MA-XRF signals do not exhibit significant variation after a certain thickness as they become infinitely thick from the point of the discussed XRF line (Figure 4b–d). For both hydrocerussite and azurite, the SWIR RIS signals show a substantial improvement in penetration of overlying paint layers when compared to the corresponding MA-XRF fluorescence lines (Values for paint layer escape depth for MA-XRF presented in Figure S12). The SWIR RIS signals are attenuated, but not as strongly as the MA-XRF signals, although the level of attenuation depends on the nature of the overlying layer, as yellow ochre layers seem to block more of the signal than the other two paints.

As previously mentioned, there is an issue where SWIR RIS misidentifies higher densities of azurite as low amounts of hydrocerussite. In the case of pure blue verditer samples, the problem is so pronounced that the hydrocerussite signal they present falls slightly above the calculated LOD, as can be seen in the central and right areas of Figure 4f. Figure 8 shows a spectral example of this issue. The cause seems to be a small peak around 1420 nm which is fit as a combination of the support and hydrocerussite components. This peak is likely a contribution of the support material and only causes issues with azurite samples as the other two pigments have features that either fully or partially cover this peak.

Regarding the semi-quantitative analysis, when directly comparing the relationships between the signals of both methods and the associated pigment areal densities (Figure 7), it can be seen that the SWIR RIS signals exhibit a much larger linear range than the MA-XRF ones. However, certain MA-XRF lines, like Pb-M, exhibit a strong linear correlation to pigment areal density, but these are limited to surface-specific information (roughly top 13 μm). Their usefulness for the quantification of multi-layer paint systems is therefore limited, especially as overlying varnish layers can further dampen the signal. The relatively poor LODs for SWIR RIS show that it is less suitable for quantification of the pigments when present in low amounts. However, in these regions, the MA-XRF signal still exhibits a roughly linear relation with pigment areal density, and therefore the two methods can be used complementarily to achieve a broader quantification range.

In the test of the painting (Figure 6), significant differences can be seen between the MA-XRF and SWIR RIS signals. The maps of hydrocerussite (Figure 6f) and Pb-M (Figure 6c) have some differences, namely the black clothing and pupils of the figure, and some background elements, like the window wall and the bridge, all of which exhibit a Pb-M signal, but no hydrocerussite signal, implying either the presence of Pb in a form different from hydrocerussite or the presence of a strongly IR absorbing compound which is masking the hydrocerussite signal. Certain areas in the background exhibit a hydrocerussite and Pb-L signal (Figure 6b), but no significant Pb-M signal. This indicates that a lead white layer is present underneath; the surface paint layer(s) absorb(s) the low energy Pb-M radiation but do(es) not strongly absorb IR radiation. Some of these areas also exhibit a Cu-K signal and have a dark green color, which would imply the presence of a Cu-based pigment layer on top of an underlying lead white layer, most likely malachite or verdigris, given the lack of an azurite signal. The spatial correlation of the hydrocerussite signals below the LOD shows that how LODs are currently described may not be entirely appropriate for this kind of (spatial) data, as the calculations ignore the spatial components and neighborhood relationships within the data. Defining a new limit that considers both spatial and spectral data, a limit of detection for imaging, would be perhaps more appropriate.

Comparing the Cu-K (Figure 6d) and azurite (Figure 6e) maps yields similar deviations. Whilst Cu-K signals are present throughout the outdoor background as well as the figure clothing, the azurite is only present in the sky, water, and rearmost trees, which are the bluer areas of the background. The differences in the background can be attributed to the use of another (green)

Cu-based pigment. The difference in the clothing could be attributed to the use of a Cu-based pigment mixed in with the primary black pigment, or the use of a Cu-based dryer, like verdigris, to reduce the long drying times common to black paints.

The gypsum signal (Figure 6g) is also of interest due to its strong correlation with the hydrocerussite signal. This could be due to a misfitting of the two features, as the most prominent of the gypsum features is the one that directly overlaps the hydrocerussite —OH feature. However, it is known from cross-section samples that there is gypsum present in the ground layer of the painting. What could be happening is more a negative correlation with the darker areas of the painting. In these areas, the more strongly IR-absorbing paints block the ground layer gypsum signal, which is mostly unobstructed in the brighter areas of the painting, which happens to be where lead white is most prominently used.

Using the relations between RIS signal intensity and pigment areal densities derived from the paint samples, the average pigment areal densities of certain areas of the painting are calculated. Based on the paints prepared for the mock-up samples, these areal densities can also be converted to the equivalent layer thickness of a single pigment paint layer, to facilitate direct comparison to the paint mock-ups, but they are not actual measurements of the layer thickness in the painting. The target areas are marked in Figure 6a. For lead white, the sky (area 1) has a pigment areal density of 21.4 mg/cm$^2$ (the equivalent of a 36 µm layer of pure lead white paint), the face (area 3) has 19.7 mg/cm$^2$ (33 µm), the background water (area 4) has 10.28 mg/cm$^2$ (17 µm), and the grass (area 5) has 8.16 mg/cm$^2$ (14 µm). For azurite, the sky (area 1) has a pigment areal density of 16.1 mg/cm$^2$ (the equivalent of a 50 µm layer of pure blue verditer paint), the background trees (area 2) have 12.4 mg/cm$^2$ (38 µm), and the background water (area 4) has 20.1 mg/cm$^2$ (62 µm). All these areas present the considered pigments in either mixture with other pigments or as underlayers and have average areal densities above the LODs and values within the common areal density values described earlier.

The achieved results of the novel SWIR RIS data processing method in both specially prepared samples and historical samples show promise in the general applicability of the method for mapping the considered pigments. The production of reasonable chemical distribution maps using standard fitting features based on reference materials provides an improvement in both reproducibility and automation over the highly dataset-specific methods currently used for RIS data processing. However, it is also clear that the method suffers when dealing with reflectance features with a strong overlap, like hydrocerussite and gypsum.

## 5 | CONCLUSION

The results achieved using MA-XRF and the proposed SWIR RIS data processing method, focusing on characteristic absorption features in specific spectral regions, have shown their potential for both pigment identification and semi-quantitative mapping in a more automated and easily reproducible fashion than the more commonly used endmember-based RIS data processing methods. If properly streamlined, the process can be reduced to roughly 15–20 min of computational time, which does not require user intervention. The application of the SWIR RIS method on the prepared paint mock-ups shows an ability to identify the considered pigments more conclusively than with only MA-XRF, albeit with comparatively poor LODs. However, the ability of the SWIR RIS method to differentiate between samples with high pigment concentration and layer thickness shows a greater information depth than that achieved with MA-XRF.

The strong correlation between the SWIR RIS signal intensity and pigment areal density shows great potential for semi-quantitative analysis, but the relatively poor LODs mean it is less suitable for low pigment areal densities. The exploration of the relationship between signal intensity and pigment areal density is limited by the fact that the pigment areal density values used were assumptions based on the amounts mixed during the preparation of the paints, and not directly measured from the prepared sample. The analysis of the samples using x-ray powder diffraction (XRPD), which provides relatively robust quantitative analysis of inorganic compounds, could provide more accurate pigment densities with which to better define their relationship to SWIR RIS signal intensities. However, the complex absorption effects that happen within a paint layer in the SWIR range make full quantification very difficult and remain a major limitation of the method.

The application of the method on the three objects studied highlights a few issues that must be overcome before the method can be considered sufficiently reliable, the primary being the possibility of overlapping features from different compounds. Some of these issues might be overcome by the inclusion of a greater number of characteristic RIS features in the fitting procedure. For example, azurite presents two other absorption features in the SWIR range at 2245 and 2351 nm. Expanding the method to fit those features as well would make the azurite maps more reliable.

Moreover, some of these shortcomings could also be addressed with a combined MA-XRF and RIS approach. Whilst MA-XRF is very reliable at identifying the elemental presence, there is only so much information that can be extracted from these results, in particular when

dealing with different pigments that have the same elemental footprint. And while this RIS method can fail if several compounds with overlapping features are present, the likelihood of these pigments also having the same elemental footprint is low, as is the case between gypsum and azurite. Moreover, absorption effects are much better understood for XRF, which could help increase the reliability for quantitative analysis. The difference in information depth alongside differences in calculated areal densities between the two methods could also provide valuable insight into paint layer stratigraphy, assisting in the identification of areas of interest for further analysis. Further development and refinement of such a multimodal method would be very beneficial to the reliability and repeatability of pigment identification procedures.

Another possible area of development is the use of the Gaussian fitting method for the analysis of RIS data in other spectral ranges. While pigments often lack reflectance features in visible to near-infrared range (VNIR, 400–1000 nm) that could be fit with this method, the mid-infrared range (MIR, 2500–25,000 nm) is rich in these kinds of features.[40] MIR RIS is not currently a commonly used method in the analysis of cultural heritage objects, but as advances in MIR spectrometers make their use more practical in museum contexts, the method is likely to become more relevant and the development of data processing methods well-suited for the analysis of artist's pigments will be of great interest.

However, whilst the method shows promise for its applicability for the identification of other pigments based on prominent and characteristic reflectance features, it is inherently limited to pigments that exhibit such prominent features, and it must be tailored to these specific features. This method should not be seen as a universal solution for the question of RIS data processing, but as an automation tool for specific common questions often addressed using RIS. A practical implementation of this method would allow non-expert users to produce specific pigment distribution maps with a comparable or lower amount of effort than that required for the acquisition of MA-XRF maps. This would be a significant improvement in both speed and reproducibility over the highly labor-intensive methods in use currently.

## ACKNOWLEDGMENTS

## DATA AVAILABILITY STATEMENT

The data that support the findings of this study are available from the corresponding author upon reasonable request.

## ORCID

*Luís Manuel de Almeida Nieto* https://orcid.org/0000-0003-2748-3906

*Francesca Gabrieli* https://orcid.org/0000-0001-7510-8719

*Annelies van Loon* https://orcid.org/0000-0001-9950-7933

*Victor Gonzalez* https://orcid.org/0000-0003-3243-7664

*Raf Van de Plas* https://orcid.org/0000-0002-2232-7130

*Matthias Alfeld* https://orcid.org/0000-0001-7974-9564

## REFERENCES

[1] M. Alfeld, L. de Viguerie, *Spectrochim Acta Part B At Spectrosc* **2017**, *136*, 81. https://doi.org/10.1016/j.sab.2017.08.003

[2] J. K. Delaney, K. A. Dooley, A. van Loon, A. Vandivere, *Herit Sci* **2020**, *8*(1), 1. https://doi.org/10.1186/s40494-019-0348-9

[3] F. Gabrieli, J. K. Delaney, R. G. Erdmann, V. Gonzalez, A. van Loon, P. Smulders, R. Berkeveld, R. van Langh, K. Keune, *Sensors* **2021**, *21*(20), 1. https://doi.org/10.3390/s21206855

[4] J. K. Delaney, D. M. Conover, K. A. Dooley, L. Glinsman, K. Janssens, M. Loew, *Herit Sci* **2018**, *6*(1), 1. https://doi.org/10.1186/s40494-018-0197-y

[5] E. Herens, C. Defeyt, P. Walter, D. Strivay, *Herit Sci* **2017**, *5*(1), 1. https://doi.org/10.1186/s40494-017-0127-4

[6] P. A. Favero, J. Mass, J. K. Delaney, A. R. Woll, A. M. Hull, K. A. Dooley, A. C. Finnefrock, *Herit Sci* **2017**, *5*(1), 1. https://doi.org/10.1186/s40494-017-0126-5

[7] M. L. Clarke, F. Gabrieli, K. L. Rowberg, A. Hare, J. Ueda, B. McCarthy, J. K. Delaney, *Herit Sci* **2021**, *9*(1), 1. https://doi.org/10.1186/s40494-021-00497-1

[8] K. A. Dooley, D. M. Conover, L. D. Glinsman, J. K. Delaney, *Angewandte Chemie-International Edition* **2014**, *53*(50), 13775. https://doi.org/10.1002/anie.201407893

[9] N. de Keyser, F. Broers, F. Vanmeert, S. de Meyer, F. Gabrieli, E. Hermens, G. van der Snickt, K. Janssens, K. Keune, *Sci. Adv.* **2022**, *8*(23), eabn6344. https://doi.org/10.1126/sciadv.abn6344

[10] R. Van Grieken, A. Markowicz, *Handbook of X-Ray Spectrom*, CRC Press, Boca Raton **2001**. https://doi.org/10.1201/9780203908709

[11] C. Cucci, E. K. Webb, A. Casini, M. Ginanni, E. Prandi, L. Stefani, T. Vitorino, M. Picollo, *Journal of the American Institute for Conservation* **2019**, *58*(1–2), 16. https://doi.org/10.1080/01971360.2018.1543102

[12] F. Pottier, M. Gerardin, A. Michelin, M. Hébert, C. Andraud, *C. R. Phys.* **2018**, *19*(7), 599. https://doi.org/10.1016/j.crhy.2018.09.007

[13] S. Ramsey, T. Mayo, S. G. Lambrakos, *J Electromagn Waves Appl* **2017**, *31*(15), 1508. https://doi.org/10.1080/09205071.2017.1352541

[14] A. Polak, T. Kelman, P. Murray, S. Marshall, D. Stothard, N. Eastaugh, F. Eastaugh, *Journal of Spectral Imaging* **2016**, *5*-(July), 1. https://doi.org/10.1255/jsi.2016.a2

[15] F. Gabrieli, K. A. Dooley, J. G. Zeibel, J. D. Howe, J. K. Delaney, *Angewandte Chemie-International Edition* **2018**, *57*(25), 7341. https://doi.org/10.1002/anie.201710192

[16] E. Pouyet, N. Rohani, A. K. Katsaggelos, O. Cossairt, M. Walton, *Pure Appl. Chem.* **2018**, *90*(3), 493. https://doi.org/10.1515/pac-2017-0907

[17] M. Picollo, C. Cucci, A. Casini, L. Stefani, *Sensors* **2020**, *20*(10), 2843. https://doi.org/10.3390/s20102843

[18] M. Vermeulen, K. Smith, K. Eremin, G. Rayner, M. Walton, *Spectrochim Acta A Mol Biomol Spectrosc* **2021**, *252*, 119547. https://doi.org/10.1016/j.saa.2021.119547

[19] C. Cucci, J. K. Delaney, M. Picollo, *Acc. Chem. Res.* **2016**, *49*(10), 2070. https://doi.org/10.1021/acs.accounts.6b00048

[20] J. K. Delaney, J. G. Zeibel, M. Thoury, R. Littleton, M. Palmer, K. M. Morales, E. R. Rie, A. Hoenigswald, *Appl. Spectrosc.* **2010**, *64*(6), 584. https://doi.org/10.1366/000370210791414443

[21] E. Pouyet, T. Miteva, N. Rohani, L. de Viguerie, *Sensors* **2021**, *21*(18), 6150. https://doi.org/10.3390/s21186150

[22] N. Rohani, E. Pouyet, M. Walton, O. Cossairt, A. K. Katsaggelos, *Angewandte Chemie International Edition* **2018**, *57*(34), 10910. https://doi.org/10.1002/anie.201805135

[23] T. Kleynhans, C. M. Schmidt Patterson, K. A. Dooley, D. W. Messinger, J. K. Delaney, *Herit Sci* **2020**, *8*(1), 1. https://doi.org/10.1186/s40494-020-00427-7

[24] T. Kleynhans, D. W. Messinger, J. K. Delaney, *Microchemical Journal* **2020**, *157*, 104934. https://doi.org/10.1016/j.microc.2020.104934

[25] R. J. Gettens, H. Kühn, W. T. Chase, *Studies in Conservation* **1967**, *12*(4), 125. https://doi.org/10.1179/sic.1967.013

[26] N. Eastaugh, V. Walsh, T. Chaplin, R. Siddall, *The Pigment Compendium*, Elsevier Butterworth-Heineman, Oxford **2004**. https://doi.org/10.4324/9780080473765

[27] S. de Meyer, F. Vanmeert, R. Vertongen, A. van Loon, V. Gonzalez, J. Delaney, K. Dooley, J. Dik, G. van der Snickt, A. Vandivere, K. Janssens, *Sci. Adv.* **2019**, *5*(8), eaax1975. https://doi.org/10.1126/sciadv.aax1975

[28] K. A. Dooley, S. Lomax, J. G. Zeibel, C. Miliani, P. Ricciardi, A. Hoenigswald, M. Loew, J. K. Delaney, *Analyst* **2013**, *138*(17), 4838. https://doi.org/10.1039/C3AN00926B

[29] C. Miliani, F. Rosi, A. Daveri, B. G. Brunetti, *Appl. Phys. A: Mater. Sci. Process.* **2012**, *106*(2), 295. https://doi.org/10.1007/s00339-011-6708-2

[30] R. L. Frost, E. Mako, J. Kristóf, T. Kloprogge, *Spectrochimica Acta Part A Molecular and Biomolecular Spectroscopy* **2002**, *58*(13), 2849. https://doi.org/10.1016/S1386-1425(02)00033-1

[31] M. Alfeld, J. V. Pedroso, M. van Eikema Hommes, G. van der Snickt, G. Tauber, J. Blaas, M. Haschke, K. Erler, J. Dik, K. Janssens, *J. Anal. At. Spectrom.* **2013**, *28*(5), 760. https://doi.org/10.1039/C3JA30341A

[32] M. Alfeld, K. Janssens, *J. Anal. At. Spectrom.* **2015**, *30*(3), 777. https://doi.org/10.1039/C4JA00387J

[33] V. A. Solé, E. Papillon, M. Cotte, P. Walter, J. Susini, *Spectrochim Acta Part B At Spectrosc* **2007**, *62*(1), 63. https://doi.org/10.1016/j.sab.2006.12.002

[34] K. Danzer, *Analytical Chemistry: Theoretical and Metrological Fundamentals*, 1st ed., Springer, Berlin Heidelberg **2007**. https://doi.org/10.1007/978-3-540-35990-6

[35] M. Alfeld, S. Pedetti, P. Martinez, P. Walter, *C. R. Phys.* **2018**, *19*(7), 625. https://doi.org/10.1016/j.crhy.2018.08.004

[36] C. G. Ryan, E. Clayton, W. L. Griffin, S. H. Sie, D. R. Cousens, *Nuclear Inst. And Methods in Physics Research, B* **1988**, *34*(3), 396. https://doi.org/10.1016/0168-583X(88)90063-8

[37] G. van der Snickt, S. Legrand, I. Slama, E. van Zuien, G. Gruber, K. van der Stighelen, L. Klaassen, E. Oberthaler, K. Janssens, *Microchem. J.* **2018**, *138*(2018), 238. https://doi.org/10.1016/j.microc.2018.01.019

[38] N. Salvadó, S. Butí, M. A. G. Aranda, T. Pradell, *Anal. Methods* **2014**, *6*(11), 3610. https://doi.org/10.1039/C4AY00424H

[39] V. Gonzalez, A. Van Loon, S. WT Price, P. Noble, K. Keune, *J. Anal. At. Spectrom.* **2020**, *35*(10), 2267. https://doi.org/10.1039/D0JA00169D

[40] F. Gabrieli, K. A. Dooley, M. Facini, J. K. Delaney, *Sci. Adv.* **2019**, *5*(8), eaaw7794. https://doi.org/10.1126/sciadv.aaw7794

## SUPPORTING INFORMATION

Additional supporting information can be found online in the Supporting Information section at the end of this article.